Progress In Electromagnetics Research, Vol. 136, 327–367, 2013

DESIGN OPTIMIZATION AND ANALYSIS OF AFPM SYNCHRONOUS MACHINE INCORPORATING POWER DENSITY, THERMAL ANALYSIS, AND BACK-EMF THD

Solmaz Kahourzade[1], Ali Gandomkar[2], Amin Mahmoudi[1], Nasrudin Abd Rahim[1], Wooi Ping Hew[1], and Mohammad N. Uddin[3]

[1]UM Power Energy Dedicated Advanced Centre (UMPEDAC), University of Malaya, Kuala Lumpur, Malaysia

[2]Power Conversion Laboratory, Yeungnam University, Gyeongsan-si, Korea

[3]Department of Electrical Engineering Lakehead University, Thunder Bay, Ontario P7B 5E1, Canada

Abstract—This paper presents the design and analysis of an inside-out axial-flux permanent-magnet (AFPM) synchronous machine optimized by genetic algorithm (GA) based sizing equation, finite element analysis (FEA) and finite volume analysis (FVA). The preliminary design is a 2-pole-pair slotted TORUS AFPM machine. The designed motor comprises sinusoidal back-EMF waveforms, maximum power density and the best heat removal. The GA is used to optimize the dimensions of the machine in order to achieve the highest power density. Electromagnetic field analysis of the candidate machines from GA with various dimensions is then put through FEA in order to obtain various motor characteristics. Based on the results from GA and FEA, new candidates are introduced and then put through FVA for thermal behavior evaluation of the designed motors. Techniques like modifying the winding configuration and skewing the permanent magnets are also investigated to attain the most sinusoidal back-EMF waveform and reduced cogging torque. The performance of the designed 1 kW, 3-phase, 50 Hz, 4-pole AFPM synchronous machine is tested in simulation using FEA software. It is found that the simulation results fully agree with the designed technical specifications. It is also found from FVA results that the motor temperature reaches

Received 2 December 2012, Accepted 8 January 2013, Scheduled 20 January 2013

* Corresponding author: Amin Mahmoudi (amaminmahmoudi@gmail.com).

at highest temperature to 87°C at the rated speed and full load under steady state condition.

1. INTRODUCTION

Permanent-magnet motors have garnered considerable interest due to their high performance [1]. Lower prices of high-energy permanent magnets and electronics used in motor fabrication also promote utilization of the motors in a wide range of applications [2]. Permanent-magnet motors come in different geometries, among which is a disc-type or axial-flux permanent-magnet (AFPM) motor available in various configurations [3–7]. The AFPM motor's high torque-to-volume ratio, excellent efficiency and flat structure are especially suited to military and transport applications, and motivate researchers to develop new approaches to design AFPM machines [8, 9]. The AFPM machines can be single- or double-sided, with or without armature slots/core, have internal/external permanent-magnet rotors, contain a surface-mounted or interior permanent magnet, and are single- or multi-staged [10]. The AFPM motor cogging torque is normally much higher as compared to conventional motors [11]; however, they can still be potentially applied to high-torque applications such as ship propulsion or flywheel energy storage systems [12, 13]. The double-sided AFPM motor type is the most promising and widely used. Topologies for double-sided AFPM machines are axial-flux one-stator-two-rotor (this structure is a type of TORUS) and two-stator-one-rotor, which is known as axial-flux interior rotor (AFIR) [14], while either of the two arrangements (external stator or external rotor) is practical. The external-stator arrangement uses fewer permanent magnets but at the expense of winding. However, the external-rotor arrangement is considered especially advantageous where the space is limited, mechanical robustness is required and torque-to-volume ratio is crucial [15]. The double-sided slotted TORUS AFPM motors are the most frequently applied among the other configurations, chiefly because they are mechanically stronger and have higher power density [16]. Therefore, the design of a TORUS AFPM machine is considered in this work.

Researchers have already reported some design techniques for both radial-flux permanent-magnet (RFPM) and axial-flux permanent-magnet (AFPM) machines [17–20]. In [17], Huang et al. derived the general sizing equation and the power density equation for RFPM machines, which was a systematic method comparing the capabilities of various topology machines. In [18], the same authors developed the sizing equation for AFPM machines but did not optimize the

design of the machine. Aydin et al. have developed optimum-sized AFPM machines for both TORUS and AFIR topologies, but only two parameters (diameter ratio and air-gap flux density) were considered as optimization variables, with optimization done through the shape modification [19, 20]. However, for proper design optimization of the machine, multiple parameters must be considered. Moreover, in all shape-modification methods, there are trade-offs among the performance parameters and the methods are inapplicable to the multi-objective optimization problems. In some studies the optimized value of $1/\sqrt{3} \approx 0.58$ for the ratio (λ) of inner diameter to the outer diameter was chosen in order to maximize the output power in AFPM machines [21, 22]. In [23], a method to reduce the free design parameters, in order to make a simple parametric study and to obtain an improved design for an AFPM machine equipped with concentrated winding was proposed and the most relevant figures of merit were theoretically analyzed by means of some parametric analysis. Recently in [24], authors provided a design based on GA method for variable speed AFPM synchronous generator considering practical limitations. However, the design methodology is not clear and the analysis of the designed machine is very limited as they did not provide any results on power density, efficiency, and total harmonic distortion (THD) of the induced voltage. Therefore, in this work the minimization of the machine size with various parameters considerations such as, winding turns, winding coefficient, electrical loading, air-gap length, diameter ratio, air-gap flux density, stator-slot number, permanent-magnet skewing, and thermal capability is performed.

The design optimization of a 1 kW, 3-phase, 50 Hz, 4-pole AFPM synchronous motor is done in this paper utilizing GA based on the motor sizing equation and practical limitations. The design objectives are considered as maximum power density, less cogging torque, best heat dissipation and minimum THD of the induced EMF. The various motor characteristics of the designed motor is then obtained through electromagnetic field analysis using FEA software. Based on the results from GA and FEA, new candidates are introduced and then put through FVA for thermal behavior prediction of the designed motor. Various winding configurations and skewing the permanent magnets are also investigated to get the most sinusoidal back-EMF and reduced cogging torque. In order to verify the design, the performance of the proposed designed 1 kW, 3-phase, 50 Hz, 4-pole AFPM synchronous machine is tested in simulation using FEA software. It is found from results that the designed machine can meet the design specifications.

2. SIZING EQUATION

The main dimensions of each electrical machine are determined by the electrical-machine-output power equation. Assuming negligible leakage inductance and resistance, the machine output power is expressed as [17]:

$$P_{out} = \eta \frac{m}{T} \int_0^T e(t) \cdot i(t) dt = m K_p \eta E_{pk} I_{pk} \tag{1}$$

where $e(t)$ is the phase air-gap EMF, $i(t)$ the phase current, η the machine efficiency, m the number of machine phases, and T the period of one EMF cycle. E_{pk} and I_{pk} are peaks of phase air-gap EMF and current, respectively. K_p is the electrical power waveform factor, defined as:

$$K_p = \frac{1}{T} \int_0^T \frac{e(t) \cdot i(t)}{E_{pk} \cdot I_{pk}} dt = \frac{1}{T} \int_0^T f_e(t) \cdot f_i(t) dt \tag{2}$$

where $f_e(t) = e(t)/E_{pk}$ and $f_i(t) = i(t)/I_{pk}$ are the expressions for normalized EMF and current waveforms. For the current effect,

Table 1. Typical prototype waveforms.

Model	*e (t)*	*i (t)*	K_i	K_p
sinusoidal	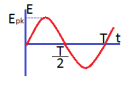	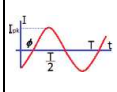	$\sqrt{2}$	0.5cosφ
sinusoidal	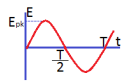	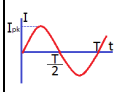	$\sqrt{2}$	0.5
rectangular	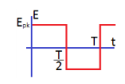	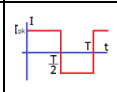	1	1
trapezoidal	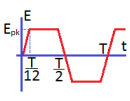	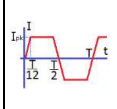	1.134	0.777
triangular	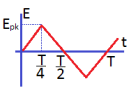	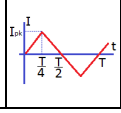	$\sqrt{3}$	0.333

current waveform factor (K_i) is defined as:

$$K_i = \frac{I_{pk}}{I_{rms}} = \frac{1}{\sqrt{\frac{1}{T}\int_0^T \left(\frac{i(t)}{I_{pk}}\right)^2 dt}} \tag{3}$$

where I_{rms} is the phase-current *rms* value. Table 1 lists typical waveforms and their corresponding power-waveform factor (K_p) and the current-waveform factor (K_i) [17]. The peak value of the phase-air-gap EMF for the AFPM machine in Equation (1) is [18]:

$$E_{pk} = K_e N_{ph} B_g \frac{f}{p}\left(1-\lambda^2\right) D_o^2 \tag{4}$$

K_e is the EMF factor which incorporates winding distribution factor (K_w) and per-unit portion of air-gap area-total spanned by the machine's salient poles (if any) [18]; N_{ph} is the number of winding turns per phase; B_g is the flux density in air-gap; f is the converter frequency; p is the machine pole pairs; λ is the AFPM machine's diameter ratio D_i/D_o; D_o is the machine's outer surface diameter; D_i is the machine's inner surface diameter. The peak phase current for Equation (1) is [18]:

$$I_{pk} = A\pi\, K_i \frac{1+\lambda}{2}\frac{D_o}{2m_1 N_{ph}} \tag{5}$$

where m_1 is the number of phases of each stator and A the total electrical loading. A general-purpose sizing equation for AFPM machines is [18]:

$$P_{out} = \frac{1}{1+K_\phi}\frac{m}{m_1}\frac{\pi}{2} K_e K_i K_p K_L \eta B_g A \frac{f}{p}\left(1-\lambda^2\right)\left(\frac{1+\lambda}{2}\right) D_o^2 L_e \tag{6}$$

where L_e is the machine's effective axial length, K_ϕ the electrical loading ratio on rotor and stator, and K_L the aspect ratio coefficient with respect to a specific machine structure and keeping in view the consequence of loss, temperature rise, and design efficiency requirements. The machine power density for volume total is defined as:

$$P_{den} = \frac{P_{out}}{\frac{\pi}{4} D_{tot}^2 L_{tot}} \tag{7}$$

where D_{tot} and L_{tot} are the machine's total outer diameter and total length respectively, including the stack's outer diameter and end-winding protrusion from radial and axial iron stacks. The generalized sizing equation approach can be readily applied to a double-sided AFPM TORUS-type machine. The outer surface diameter (D_o) can be written as:

$$D_o = \sqrt[3]{\frac{P_{out}}{\frac{\pi}{2}\frac{m}{m_1} K_e K_p K_i A B_g \eta \frac{f}{p}\left(1-\lambda^2\right)\left(\frac{1+\lambda}{2}\right)}} \tag{8}$$

The machine's total outer diameter (D_{tot}) for the TORUS motor is:

$$D_{tot} = D_o + 2W_{cu} \tag{9}$$

where W_{cu} is the end winding protrusion from the iron stack in radial direction. For back-to-back wrapped winding, protrusions occur towards the machine's axis as well as outsides, and can be calculated as:

$$W_{cu} = \frac{D_i - \sqrt{D_i^2 - \frac{2AD_{ave}}{K_{cu}J_s}}}{2} \tag{10}$$

where D_{ave} is the machine's average diameter, J_s the current density, and K_{cu} the copper-fill factor. The machine's axial length (L_e) is given by:

$$L_e = L_s + 2L_r + 2g \tag{11}$$

where L_r is the rotor's axial length, and g is the air-gap length. The stator's axial length (L_s) is:

$$L_s = L_{cs} + 2L_{ss} \tag{12}$$

For the slotted machines, the stator slot depth is $L_{ss} = W_{cu}$, and the stator core's axial length (L_{cs}) is:

$$L_{cs} = \frac{B_g \pi \alpha_p D_o (1+\lambda)}{4pB_{cs}} \tag{13}$$

where B_{cs} is the stator-core flux density, and α_p is the ratio of average air-gap flux density to peak air-gap flux density. The rotor's axial length (L_r) becomes:

$$L_r = L_{cr} + L_{pm} \tag{14}$$

where L_{pm} is the permanent-magnet length. The rotor core's axial length (L_{cr}) is:

$$L_{cr} = \frac{B_u \pi D_o (1+\lambda)}{8pB_{cr}} \tag{15}$$

where B_{cr} is the flux density in the rotor disc, and B_u is the attainable flux density on the permanent-magnet's surface, while the permanent-magnet length (L_{pm}) can be calculated as:

$$L_{pm} = \frac{\mu_r B_g}{B_r - \left(\frac{K_f}{K_d} B_g\right)} K_c g \tag{16}$$

where μ_r is the permanent-magnet's recoil relative permeability, B_r the permanent-magnet residual flux density, K_d the leakage flux factor, $K_f = B_{gpk}/B_g$ the peak value corrected factor of air-gap flux density in the AFPM machine's radial direction, and K_c the Carter factor.

3. GENETIC ALGORITHM AND OPTIMIZATION

Designing the highest-possible-power-density AFPM motor is basically a multi-dimensional optimization problem of achieving an objective function within many constraints. According to Equations (1) to (16), parameters often affect each other, varying simultaneously (for example D_i, D_o, and λ); therefore, the AFPM machine optimization is a non-linear problem. GA is a strong tool that can solve various complex and non-linear optimization problems [25, 26]. GA may thus provide many answers for problem optimization due to its parallel search capability. However, most other algorithms are not in parallel and are only capable of simultaneously solving problems in just one direction.

This section presents the key elements of GA based design optimization incorporating practical limitations and the optimized dimensions of the machine.

3.1. Design Restrictions and Requirements

Optimally, a design would include maximum power density incorporated with desired sinusoidal back-EMF and would be maintained within design restrictions and requirements. Table 2 lists all the practical limitations and requirements for the design. The limitations are based on the typical 1 kW AFPM synchronous machine applied to scooter or any low power application with similar rating.

It is to be mentioned that in high-speed, high-torque, and low-supply-voltage applications, sine-wave machines offer many advantages [27]. Mostly for small machines, the number of poles is limited due to the reduced space available for the windings. Nevertheless, the most restricting limitation for the number of poles is the motor operation speed. If the speed is high, a large number of poles will bring an increase in the frequency, which directly leads to higher stator core losses and higher converter losses. Additionally, the cost of permanent magnets increases. Therefore, the final decision is made in favor of the 4-pole machine, with the frequency limited to 50 Hz.

3.2. Fitness Function

A key issue in genetic algorithm programming is the selection of a fitness function for obtaining the best solution to a problem [28]. An inappropriate fitness function may lead to the wrong answer. Another potential problem may arise when the produced genes are relatively better than other genes [29], and the answer may lead towards a local

Table 2. Design restrictions and requirements.

Dimensional Constraints	
machine outer diameter (D_o)	$D_o \leq 300\,\text{mm}$
inner to outer diameter ratio (λ)	$0.4 \leq \lambda \leq 0.75$
effective axial-length of the motor (L_e)	$L_e \leq 500\,\text{mm}$
air-gap length (g)	$0.5\,\text{mm} \leq g \leq 2.5\,\text{mm}$
Material Limitations	
stator and rotor core flux density (B_{cs}, B_{cr})	B_{cs}, $B_{cr} \leq B_{\max} = 1.5\,\text{T}$
permanent remanence	$1.3\,\text{T}$
permanent-magnet temperature	$\theta_{PM} \leq 120^{\circ}\text{C}$
Requirements	
rated line-to-line voltage (rms)	$V_{L\text{-}L} \leq 50\,\text{V}$
input phase current (rms)	$I_{rms} \leq 20\,\text{A}$
air-gap flux density (B_g)	$0.35\,\text{T} \leq B_g \leq 0.95\,\text{T}$
electrical loading (A)	$1000 \leq A \leq 30000$
output power (P_{nom})	$P_{nom} = 1\,\text{kW}$
pole pairs (p)	$p = 2$
motor efficiency (η)	$\eta \geq 80\%$
frequency (f)	$f = 50\,\text{Hz}$
number of phases (m)	$m = 3$

solution. The AFPM machine power density (Equation (7)) is chosen as the fitness function and is calculated for each step and chromosome. This can be overcome by choosing a large population number.

3.3. Real-Coded Genetic Algorithm (RCGA)

The GA includes operations such as reproduction, crossover, and mutations. Reproduction is a process in which a new generation of population is formed by selecting the fitness individuals in the current population. Crossover is the most dominant operator in GA. It is responsible for producing new offsprings by selecting two strings and exchanging portions of their structures. The new offsprings may replace the weaker individuals in the population. Mutation is a local operator, which is applied with a very low probability. Its function is to alter the value of random position in a string. The real-coding genetic-algorithm (RCGA), chromosome representation, crossover, and mutation operators are described as follows.

Figure 1. Chromosome representation (1×6 array).

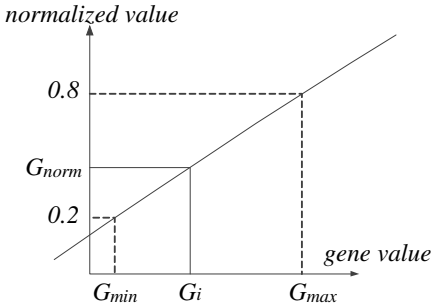

Figure 2. Real gene coding (linear normalization).

3.3.1. Chromosome Representation

Figure 1 illustrates each chromosome's 1×6-array for the proposed genetic algorithm, while B_g, λ, g, A, K_w and N_{ph} are air-gap flux density, inner to outer diameter ratio, air-gap length, electrical loading, winding coefficient, and winding turns in each phase, respectively. Every generation has a chromosome population of 1400 and gets randomly selected from the first generation.

Chromosome variables or genes have real values, and hence real coding is applied for normalizing each gene as shown in Fig. 2. Linear normalization results from:

$$G_{normal} = \frac{0.8 - 0.2}{G_{\max} - G_{\min}}(G_i - G_{\min}) + 0.2 \tag{17}$$

where G_i is the chromosome gene value varying between $G_{\min}$ and $G_{\max}$. The normalized values are limited between upper and lower limits 0.8 and 0.2, respectively.

3.3.2. Crossover

For the present research, the elitist method is used as a selection operator for two-point crossover (Fig. 3). Two random numbers between "1" and "chromosome length -1" are first generated ($1 \leq$ random number $\leq$ chromosome length -1). Each chromosome is cut from the specified points in Fig. 3, and the equivalent sections are then exchanged.

3.3.3. Mutation

In this research, mutation is executed with a probability P_m ($0.005 \leq P_m \leq 0.05$) and the outcome needs to be a valid chromosome. Table 2

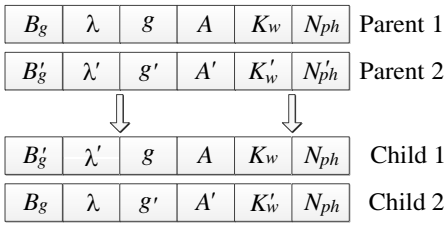

Figure 3. Two-point crossover.

lists all genes' permitted optimization variations. In real coding, for instance, genes are randomly chosen such that a random value is selected from the interval mentioned, after which it is added to, or removed from, the gene pool.

3.4. Flowchart

Figure 4 shows the flowchart for optimization using GA for the highest possible power density of the AFPM motor. GA starts with a population which is the initial set of random solutions. The population consists of chromosomes that are string-structured concatenated lists of digits which code the problem's control parameters. In this paper, a 1400-string population is randomly created and the chromosomes are normalized. Chromosomes evolve from generation to generation via successive iterations; a new generation is made by selection according to fitness value, parents and some off-springs, while others are rejected to limit the population size. Half the genes from previous steps are omitted, and a new generation is created by performing crossover and mutation on selected genes. From every two selected genes, two children are created, replacing omitted genes, thus creating a new generation with an equal population as before (1400). The stopping criterion is then verified; upon validation, the algorithm stops and the final genes are selected, otherwise, new chromosomes, or off-springs, are produced. The new generation undergoes all previous steps, and after several generations, the algorithm ends when the stopping criterion is fulfilled. Finally, appropriately selected genes optimize the motor dimensions or offer close to optimal dimensions with the highest power density.

3.5. GA Based Computed Results

For a 3-phase, 2-pole-pair AFPM motor, the potential number of stator slots is assumed to be 9, 12, 15, 18, 21, and 24; the GA program

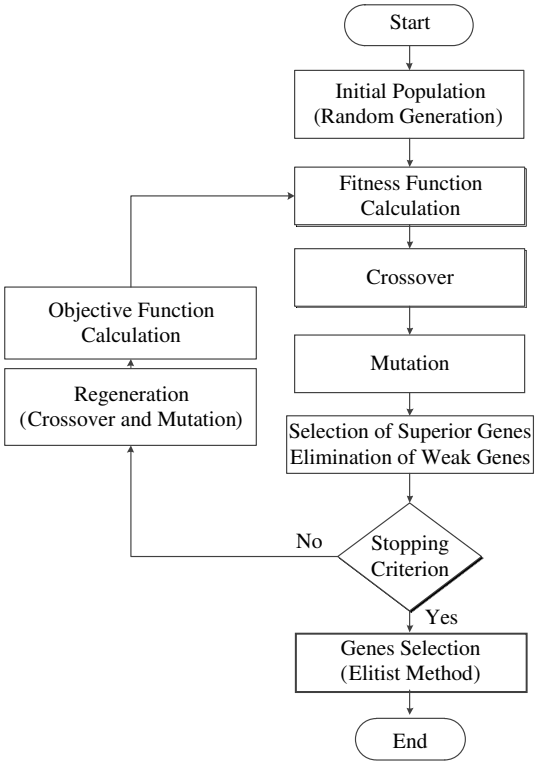

Figure 4. The flowchart for optimization using GA.

is then executed based on these stator slot numbers. The present algorithm stops when the fitness function value (Equation (7)) for the best current-population point is less than, or equals, the fitness limit ($G_{n+1} - G_n \leq \varepsilon$). An AFPM machine may have any even number of permanent-magnet poles ($2p$) and any number of stator slots (N_s). From this infinite set, only a few permanent-magnet pole and stator slot count combinations can maximize stator slot utilization and result in efficient production of torque. The number of stator slots in each pole, per pole pair, for 9, 15, 18, and 21 stator-slot counts, is fractional. The fractional slot-pitch winding configuration is more complicated than full slot-pitch, but all values are considered important because they reduce current and voltage harmonics, and also cogging torque.

Table 3 lists various motor design parameters, with various stator slot numbers optimized through GA optimization. The optimized winding configurations for different stator slot machines are also found using FEA based simulation [30]. The optimized winding

Table 3. Dimensions of the motor, with highest power density for different number of stator-slot counts obtained via GA.

No. of slots	P_{den} (W/cm^3)	D_o (mm)	N_{ph} (turns)	A (A/m)	g (mm)	L_{pm} (mm)
9	0.35	157	71	16089	1.20	4.60
12	0.35	166	64	14370	1.07	2.73
15	0.36	161	70	15198	1.10	3.60
18	0.36	158	76	16757	1.26	3.00
21	0.36	152	69	16503	1.29	3.76
24	0.36	162	67	15070	1.21	2.63
No. of slots	L_{cs} (mm)	L_{cr} (mm)	B_g (T)	λ	D_s (mm)	
9	13.44	12.9	0.49	0.52	16.90	
12	12.00	11.7	0.40	0.46	16.64	
15	13.00	13.0	0.48	0.48	15.60	
18	13.00	12.5	0.46	0.55	17.25	
21	13.30	12.8	0.51	0.50	17.90	
24	12.99	12.4	0.46	0.50	16.00	

configurations of the permanent-magnet motor simulated in this paper are given in the Appendix. As a sample, Fig. 5 shows the MATLAB-programming fitness-function variations for 120 generation (which are not fully optimized) used for optimizing the various stator slot counts.

4. FINITE ELEMENT ANALYSIS (FEA)

GA facilitates getting the maximum power density, so dimensions obtained via GA are considered raw data, thus further analysis is needed for sufficiently mature final design. 3D-FEA is employed for analyzing the double-sided TORUS AFPM motor's magnetic circuit and power density evaluation, providing an overall picture of different parts of the proposed motors saturation levels and extracting their characteristics. The fundamental FEA equations are [31]:

$$\nabla \times \vec{B} = \mu \vec{J}_s \tag{18}$$

$$\nabla \times \vec{J}_s = -\sigma \frac{d\vec{B}}{dt} \tag{19}$$

$$\vec{B} = \nabla \times \vec{\psi} \tag{20}$$

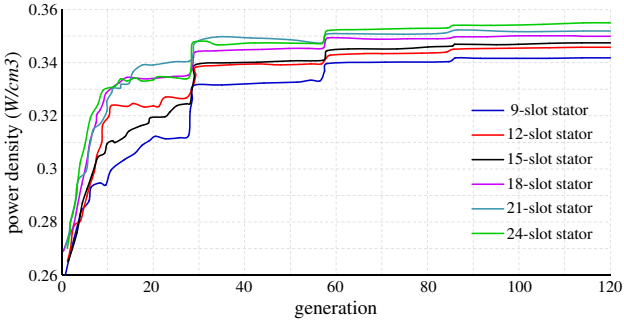

Figure 5. Fitness function variation during GA optimization.

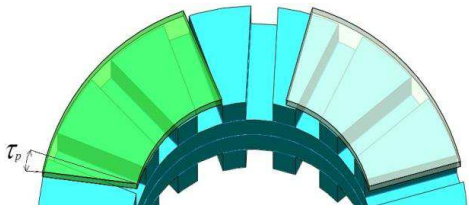

Figure 6. Permanent-magnet skew diagram for cogging torque reduction and elimination of undesired harmonic components.

where $\vec{B}$, $\vec{J}_s$, and $\vec{\psi}$ are magnetic flux density, current density, and magnetic vector potential, respectively; σ and μ are electrical conductivity and magnetic permeability. If $\vec{H}$ is taken as magnetic field intensity, the previous equations result in:

$$\nabla \times \left(\frac{1}{\sigma} \nabla \times \vec{H} \right) + \frac{\partial \vec{B}}{\partial t} = 0 \tag{21}$$

where the vector fields are represented by first-order edge elements and the scalar fields by second-order nodal unknowns. Field equations are coupled with the circuit equations for conductors and the classical Newton-Raphson method is used for solving the equations. The numerical solution of Equations (18)–(21) employs a finite element discretization approach. The AFPM motors have a unique construction; its lack of symmetry makes 3D-FEA a design requisite. An advantage of 3D-FEA is that various components of flux density can be calculated highly accurately [32–35]. The design was simulated on commercial Vector Field Opera 14.0 3D software [36].

Usually, permanent-magnet skewing is beneficial for reducing the cogging torque in electric machinery. It also eliminates some undesired harmonics, reducing the back-EMF total harmonic distortion (THD). It should be noted that the back-EMF amplitude is also reduced

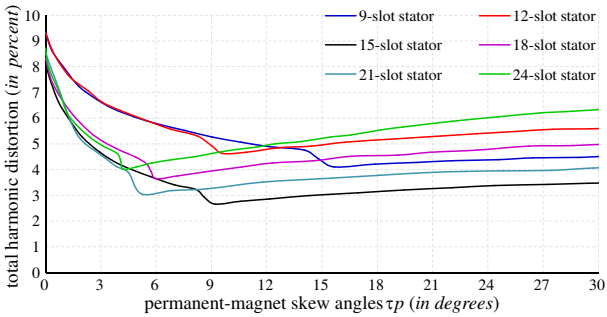

Figure 7. Back-EMF THD variation against skew angles for motors with different number of slots.

slightly with skewing. Skewing angle should be less or equal to slot pitch. Fig. 6 portrays a diagram of the permanent magnet's geometric skewing with regards to stator teeth and slots. Skew angle (τ_p) is the angle at which the rotor's permanent magnets are skewed relative to the stator teeth.

Through GA analysis, motor dimensions are obtained for each stator slot count. The FEA then provides the THD of back-EMF at various skew angles for the design candidates presented in Table 3. Fig. 7 shows THD variation against permanent-magnet skew angles. Minimum THD is clear to see for the motor with 15 stator slots and 9-degree permanent-magnet skew. So, the optimum selected chromosome is the one that represents a motor with 15 stator slots per pole pair in Table 3. It is to be mentioned that the adopted fractional winding $q = 5/4$ (slots per pole per phase) considered for back-EMF waveform analysis includes the phase coils of one entire stator side, suitably series connected.

5. FINITE VOLUME ANALYSIS (FVA)

Computational fluid dynamic (CFD) is the study of fluids dynamics and heat transfer by means of numerical methods. Various well established discretization methods are used in CFD: finite difference method (FDM), finite element method (FEM), finite volume method (FVM) [37]. The possibility of using either structured or unstructured grids have made FVM very attractive. The FVM based solvers are more computationally efficient in terms of computational speed and memory requirement [38].

GA may provide more than one answer for an optimization problem; each by considering a special parameter. This paper takes

Table 4. 10 superior chromosomes of the machine designs with 15 stator slots obtained via GA.

chromosome number	P_{den} (W/cm^3)	θ (°K)	D_o (mm)	N_{ph} (turns)	A (A/m)	g (mm)
1	0.36	371	161	70	15198	1.10
2	0.36	367	166	83	17712	1.01
3	0.36	360	170	90	14115	1.03
4	0.35	378	158	72	16280	1.30
5	0.35	365	152	69	16503	1.29
6	0.35	370	158	88	18636	1.45
7	0.35	375	168	68	14816	1.23
8	0.35	363	158	71	15802	1.55
9	0.35	372	165	72	16025	1.42
10	0.35	363	158	69	15420	1.54
chromosome number	L_{pm} (mm)	L_{cs} (mm)	L_{cr} (mm)	B_g (T)	λ	D_s (mm)
1	3.60	13.0	13.0	0.48	0.48	15.6
2	1.75	12.0	10.5	0.37	0.37	180
3	2.42	14.0	10.8	0.46	0.47	15.8
4	3.60	13.0	12.5	0.47	0.47	17.0
5	4.43	13.5	12.8	0.51	0.51	18.0
6	4.80	15.0	14.0	0.45	0.45	18.0
7	2.34	11.5	11.0	0.41	0.41	17.0
8	4.31	13.5	13.0	0.48	0.48	16.5
9	2.45	11.0	11.0	0.40	0.40	18.0
10	4.76	13.5	13.4	0.50	0.50	16.0

advantage of this feature in order to find the best heat-removal configuration of the designed motors. So, the best 10 chromosomes from GA optimization of the 15 stator-slot per pole-pair configuration are selected for further analysis. The FVA is then applied to provide the total thermal spectrum of the candidate chromosomes for the designed motors. Table 4 lists the various parameters of the designed motors with 15 stator slots per pole pair for the 10 superior chromosomes from GA optimization indicating the highest temperature at full-load under steady-state condition for each one. As per Table 4, chromosome number 3 represents the designed motor with lowest maximum temperature at full-load under steady-state condition.

The flow and heat transfer phenomena inside an AFPM motor

include the continuity equation, momentum equation, and energy equation. In the absolute velocity and vector format, the governing equations are [39]:

$$\frac{\partial \rho}{\partial t} + \nabla(\rho U) = 0 \tag{22}$$

$$\frac{\partial(\rho U)}{\partial t} + \nabla(\rho U_r U) + \Omega \times U = -\nabla Pr + \nabla(\mu_v \nabla U) \tag{23}$$

$$\frac{\partial(\rho E)}{\partial t} + \nabla\left(\rho U \cdot (\rho E + Pr)\right) = \nabla(k_{eff} \nabla\theta + \overline{\overline{\tau_{eff}}} \cdot U) \tag{24}$$

where ρ is the air density, U is the velocity vector, t is the time, Pr is the pressure, E is the enthalpy, and θ is the temperature. The air pressure, density, and temperature are governed by the ideal gas law $Pr/\rho = R\theta$ where R is the ideal gas constant. Ω is the rotation vector of the cooling fan. U_r is a vector defined by: $U_r = U - \Omega \times r$. r is the location vector in the reference frame. k_{eff} and $\overline{\overline{\tau_{eff}}}$ are effective thermal conductivity and stress tensor, respectively. The effective thermal conductivity includes molecular conductivity and the turbulence thermal conductivity ($k_{eff} = k + C_p \mu_{vt}/Pr_t$). The viscosity ($\mu_v = \mu_{v0} + \mu_{vt}$) in Equation (24) includes the molecular viscosity (μ_{v0}) and turbulence viscosity (μ_{vt}). With this set of the momentum equations, the rotation vector is introduced for the rotation of the rotors. A rotating reference approach is employed instead of the rotating sliding mesh approach. Since the rotor is rotating at a constant speed, the rotating reference frame approach gives the same numerical results while consuming much less computing power.

The turbulence viscosity is calculated by $\mu_{vt} = C_\mu \kappa^2/\varepsilon$ with an empirical constant, $C_\mu = 0.09$. The turbulence kinetic energy (κ) and dissipation rate (ε) are governed by the standard κ-ε transport equations.

$$\frac{\partial}{\partial t}(\rho k) + \nabla(\rho k U) = \nabla\left[\left(\mu + \frac{\rho C_\mu k^2}{\varepsilon \sigma_e}\right) \cdot \nabla k\right] + G_k + G_b - \rho\varepsilon - Y_M \tag{25}$$

$$\frac{\partial}{\partial t}(\rho \varepsilon) + \nabla(\rho \varepsilon U) = \nabla\left[\left(\mu_v + \frac{\rho C_\mu k^2}{\varepsilon \sigma_\varepsilon}\right) \cdot \nabla \varepsilon\right] + G_{1\varepsilon}\frac{\varepsilon}{k}(G_k + C_{3\varepsilon} G_b) - C_{2\varepsilon}\rho\frac{\varepsilon^2}{k} \tag{26}$$

The contribution of density fluctuation in the air to overall turbulence dissipation rate, $Y_M = 2\rho\varepsilon k/v_s^2$ where v_s is the speed of the sound. The generation of turbulence kinetic energy, $G_k = 2\mu_{vt}\bar{\bar{S}} \cdot \bar{\bar{S}}$. The generation of turbulence due to buoyancy force (temperature variation), $G_b =$

Table 5. Thermal properties of the solid materials in the rotor.

regions	density ρ (kg/m^3)	heat capacity C_p (J/kg/°K)	conductivity k (W/m/°K)
laminated stator	8440	377.0	$k_z = 1.12$, $k_x = k_y = 44.20$
permanent magnet	7410	430.0	14.45
rotor disc	8038	502.5	16.36
housing	8912	397.0	341.00

$-a_g \mu_{vt} \nabla\rho/(\rho Pr_t)$. $\bar{\bar{S}}$ is the mean rate of the strain tensor in the fluid and a_g is the gravitation vector.

The empirical constants, in Equations (25) and (26), are $C_{1\varepsilon} = 1.44$, $C_{2\varepsilon} = 1.92$, $\sigma_k = 1.0$, and $\sigma_\varepsilon = 1.3$. $C_{3\varepsilon}$ is calculated by $C_{3\varepsilon} = \tanh(|U_z|/\sqrt{U_x^2 + U_y^2})$ where U_x, U_y, U_z are the velocity in x, y, and z directions, respectively. In the near wall region, the turbulence parameters in the fluid and the parameters on the solid wall surface are bridged by the standard wall function.

$$\frac{\partial}{\partial t}(\rho_s h_s) + \nabla(\Omega \times r \cdot \rho h_s) = \nabla(K_s \nabla\theta) + S_s \tag{27}$$

The governing equation of heat conduction in the solid regions, in vector format, is given in Equation (27). The solid enthalpy (h_S) is defined by $h_s = \int_{\theta_{ref}}^{\theta} C_p d\theta$. The subscription s is a general representation of solid material.

S_S is the heat source in the solid, including the iron loss and the copper loss in the stator. In the stationary solid regions, the motor stator and the aluminum housing, the second term on the left hand side of Equation (27) becomes zero. Table 5 lists different material properties used in various regions of the motor.

The numerical solution of Equations (22)–(27) employs a finite volume discretization approach. The commercial software package, ANSYS-FLUENT, is used for the simulation runs [40]. The relaxation factor for the mass, momentum, energy, turbulence kinetic energy, and turbulence dissipation rate are 0.8, 0.6, 0.9, 0.8, and 0.8 respectively [41]. The iterative solution procedure continues until the residuals of the mass conservation equation, momentum conservation equation, and equations for turbulence quantities are all smaller than 10^{-4}, while the residual of the energy equation is lower than 10^{-6}.

To accurately assess the motor's thermal behavior, it is vital to calculate the heat generation due to the losses. They include copper loss (P_{cu}) and core loss (P_{cor}) components, respectively. The copper loss ($R_s \times I^2$) is responsible for most of the total losses. Stator resistance (R_s) depends on load and winding temperature [42].

$$R_s = \frac{2N_{ph\text{-}s}(l + l_e)}{\sigma_T N_{ph\text{-}p} s_{cu}} \tag{28}$$

$N_{ph\text{-}s}$ is number of winding turns in series per phase, $N_{ph\text{-}p}$ the number of winding turns in parallel per phase, σ_T the copper wire's electric conductivity at temperature θ, and s_{cu} the copper wire's cross-section. Thin parallel wires minimize the skin effect; therefore it is not considered in Equation (28). Coil length and end-winding length are l and l_e, respectively.

Hysteresis loss (P_h) and eddy current loss (P_e) comprise the motor core loss (P_{cor}) and can be calculated in terms of the Steinmetz equation as:

$$P_h = \frac{k_h \cdot B_{\max}^{\xi} \cdot f}{\rho_c} \quad \text{and} \quad P_e = \frac{k_e \cdot B_{\max}^2 \cdot f^2}{\rho_c} \tag{29}$$

k_h, k_e, $B_{\max}$, and ρ_c are hysteresis constant, eddy current constant, maximum flux density, and core material density, respectively. ζ is the hysteresis coefficient which depend on the lamination material, thickness and conductivity. The power loss data of the 0.5 mm silicon steel paper used to fit the Steinmetz equation describes the specific loss in W/kg as:

$$P_{cor} = 0.014492B^{1.8}f + 0.00004219B^2f^2 \tag{30}$$

As seen, open slots are used in the stator design due to simplicity and cheapness. They create slot harmonics causing eddy current in this rotational speed and air-gap length. These losses are also taken into account to compute the efficiency. For a fine calculation of stator core losses, FE-AC analysis is done repeatedly for each space harmonic component (up to the 49th order) in combination with the current waveform's simulated time harmonic components, to obtain the laminated-stator eddy current losses.

An axial-flux motor's stator is theoretically either laminated spirally or axially (Fig. 8). The spiral lamination is well known; however, the axial lamination of the stator, creating the slots, and to maintain the stator mechanically integral is too difficult. In this paper, spiral lamination silicon steel paper with thickness of 0.5 mm is utilized, which is quite fair as the supply frequency is 50 Hz. It is worth mention that the thinner paper (e.g., 0.1 mm sheet) may lead to poor stacking factor.

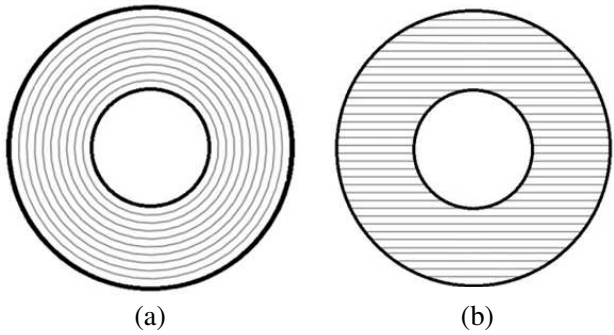

Figure 8. Spiral and axial lamination of an axial-flux motor's stator. (a) Spiral lamination. (b) Axial lamination.

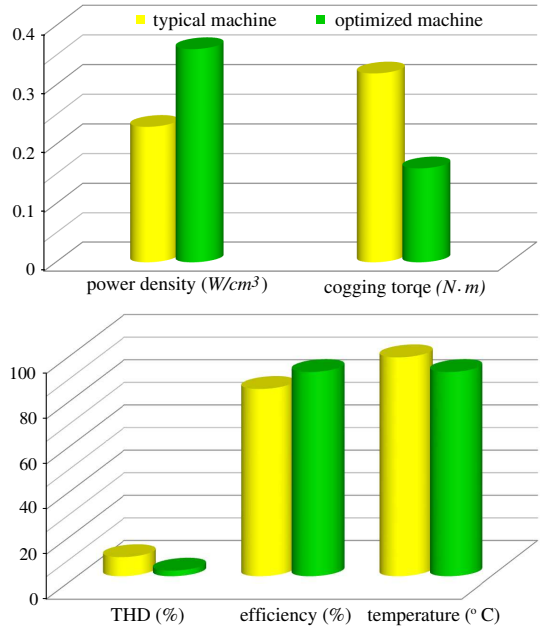

Figure 9. The characteristics of the typical and optimized machines.

6. DESIGN COMPARISON

Based on the GA, FEA, and FVA optimization, it is found that the design of 1 kW, 3-phase, 50 Hz, 15 stator-slots per pole pair with 9-degree permanent-magnet skewing achieves highest power density, low cogging torque, and minimum THD of the back-EMF. It is also found

Table 6. A typical 1 kW TORUS machine design dimensions and specifications.

nominal voltage	V_{nom}	110 V
nominal power	P_{nom}	1 kW
number of poles	$2 \times p$	4
number of phases	m	3
drive frequency	f	50 Hz
efficiency	η	83%
outer diameter	D_o	220 mm
inner diameter	D_i	130 mm
inner to outer diameter's ratio	λ	0.56
magnet's axial length	L_{pm}	7 mm
pole pitch	γ_p	140°
permanent-magnet skew angle	τ_p	0°
stator-yoke thickness	$2 \times L_{cs}$	22 mm
rotor-yoke thickness	L_{cr}	12 mm
slot width	W_s	12 mm
slot depth	D_s	12 mm
number of stator slots	$2 \times N_s$	24
number of winding turns per phase	$2 \times N_{ph}$	$(12 \times 48)/3$
air-gap flux density	B_g	0.5 T
air-gap length	g	1.5 mm

that the motor reaches its highest temperature of 87°C under rated conditions in steady-state. It would be better to verify the optimal machine design with a normal design. It illustrates how the machine characteristics are improved via optimal design. Therefore, this section compares the motor characteristics of the optimized machine with that of machine design without optimization, in terms of power density, cogging torque, THD of induced voltage, efficiency, and maximum temperature. Table 6 lists the dimensions and specifications of a typical TORUS machine with similar rating but without any optimization. Both FEA and FVA are employed to extract the machine design characteristics. Fig. 9 compares the characteristics of the optimized machine with the typical machine. It is found that all the parameters are improved considerably; however, the temperature deference is not significant. It is as a result of higher volume of the typical motor and consequently providing bigger area to dissipate the heat.

7. ELECTROMAGNETIC FIELD ANALYSIS

The best motor design dimensions are selected based on the proposed candidates from all the methods (genetic algorithm, finite element analysis, and finite volume analysis simulation). However, the final optimized design is made possible with minor changes effectuated by the powerful FEA and FVA, with the strenuous task of changing permanent-magnet thickness, air-gap length, and length of stator yoke and rotor yoke several times. Fig. 10 shows the exploded view of the designed motor which is an inside-out double-rotor single-stator axial-flux permanent-magnet motor. Table 7 lists the machine design's final dimensions and specifications.

Figure 11 shows finite element field analysis of the designed 15-

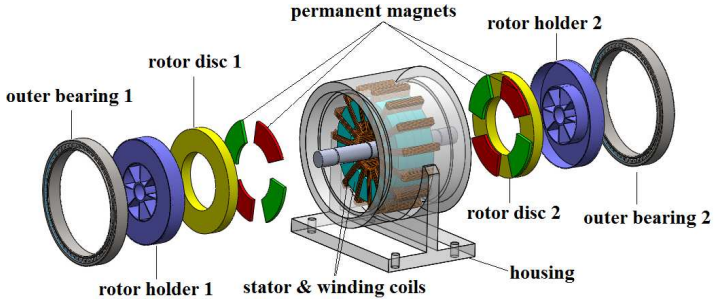

Figure 10. Exploded diagram of the designed motor.

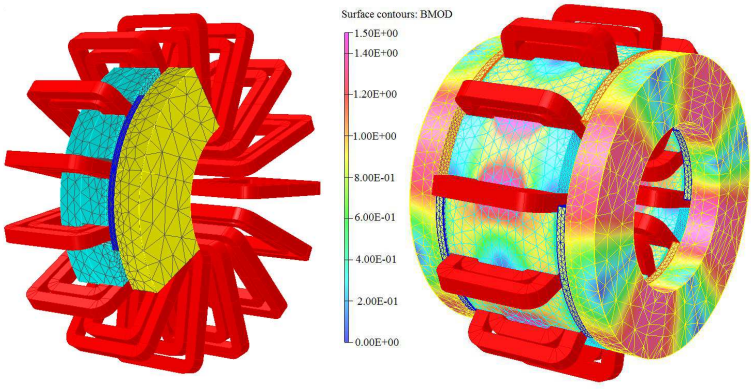

Figure 11. Field analysis of the designed AFPM motor by Vector Field Opera 14.0 software [36]. (a) 3D auto-mesh generation. (b) Flux-density plot.

Table 7. The motor's final design dimensions and specifications.

nominal voltage	V_{nom}	46 V
nominal power	P_{nom}	1 kW
number of poles	$2 \times p$	4
number of phases	m	3
drive frequency	f	50 Hz
efficiency	η	90.5%
outer diameter	D_o	170 mm
inner diameter	D_i	80 mm
inner to outer diameter's ratio	λ	0.47
magnet's axial length	L_{pm}	2.5 mm
pole pitch	γ_p	118°
permanent-magnet skew angle	τ_p	9°
stator-yoke thickness	$2 \times L_{cs}$	30 mm
rotor-yoke thickness	L_{cr}	11 mm
slot width	W_s	10 mm
slot depth	D_s	16 mm
number of stator slots	$2 \times N_s$	30
number of winding turns per phase	$2 \times N_{ph}$	$2 \times (15 \times 18)/3$
air-gap flux density	B_g	0.47 T
air-gap length	g	1 mm

stator-slot per pole pair AFPM motor. Fig. 11(a) shows one eighth of the entire motor, the part which is used to model the FEA-designed AFPM motor's structure: 90° of the half motor structure and 1 pole, fulfilling symmetry conditions. It is the portion of the meshed model, a three-dimensional auto-mesh comprising tetrahedral elements with 6 nodes fitting circular layers starting from the shaft to the outer diameter of the AFPM motor, along with entire winding configuration. It is to be noted that the adopted fractional winding ($q = 5/4$; slot/(pole $\times$ phase)) necessitate to consider the full periphery (four poles/side), in order to complete the space period. So, the entire winding is used to model the machine.

The entire machine comprises $2 \times 15 = 30$ stator slots and 2 pole-pairs. Fig. 11(b) shows the magnetic flux density distribution over different AFPM motor parts. The flux density obtained from FEA is somewhat less than theoretically calculated through GA based sizing equation due to neglected core magnetic reluctance. In fact, the flux density of different core parts decreases when the magneto-motive force (MMF) drops in real conditions.

Magnetic flux density evaluation for various sections of the designed AFPM machine is essential to detect saturation of either the core or the teeth, which decreases machine efficiency and thus

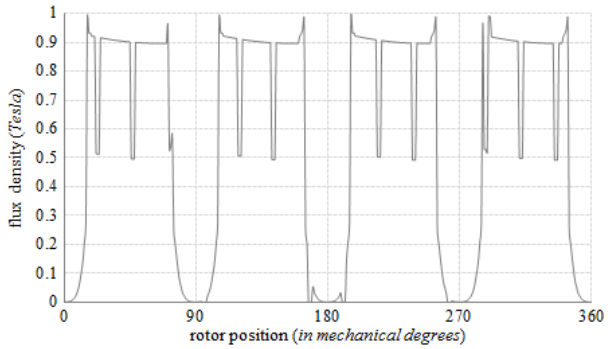

Figure 12. Air-gap magnetic flux density distribution, for average radius.

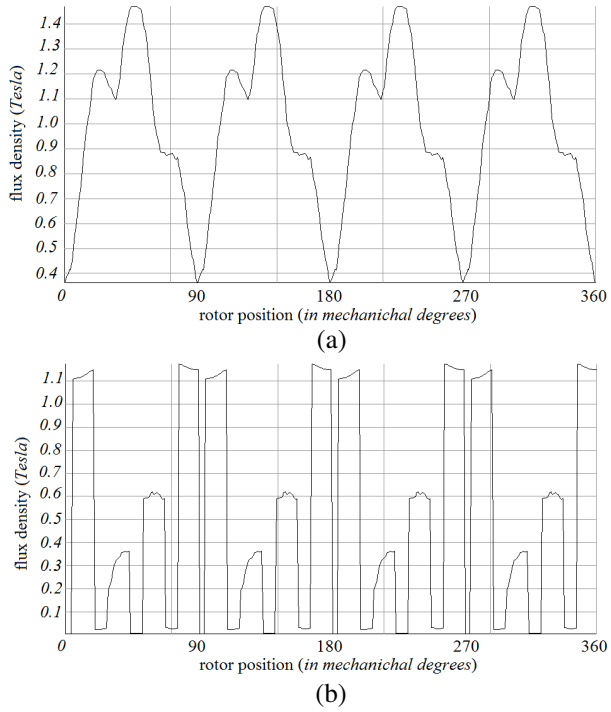

Figure 13. Stator magnetic flux density, for average radius. (a) Stator yoke. (b) Stator teeth.

affects operation. Fig. 12 shows air-gap flux density distribution with average radius. It is found from this figure that the air-gap maximum flux density is 0.94 Tesla (T), and the average is 0.47 T. Due to the progressive shift between permanent magnets and stator teeth, because of fractional winding, the flux density holes due to slots opening appear different from one pole to the others. It is obvious that the number

Table 8. Comparison of magnetic flux density between FEA based calculated and motor sizing equation based investigation.

	air-gap		stator yoke		rotor yoke		magnet surface		teeth		
	B_g		B_{cs}		B_{cr}		B_m		B_t		
	Ave.	Max.	Ave.	Max.	Ave.	Max.	Ave.	Max.			
FEA	0.47	0.94	1.20	1.5	1.4	1.45	0.5	0.9	0.36	0.59	1.1
Sizing Eq.	0.48	0.95	1.25	1.5	1.42	1.48	0.5	0.9			

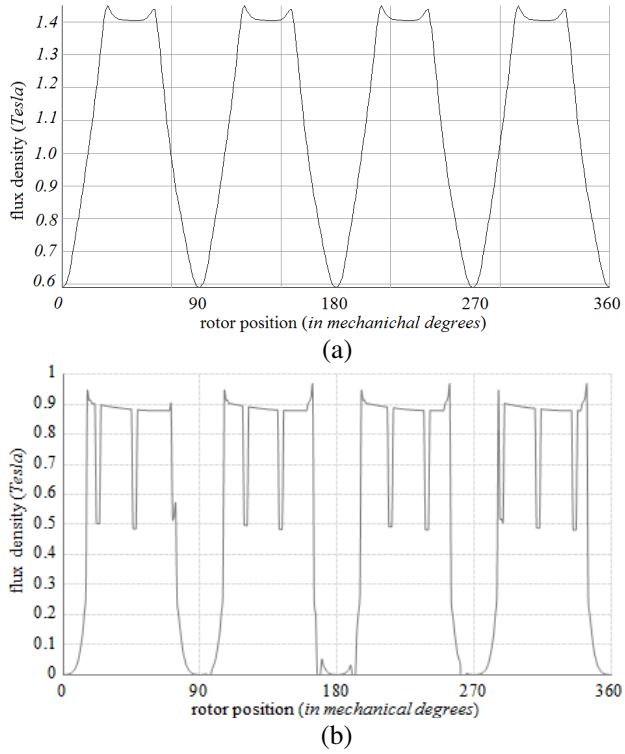

Figure 14. Rotor magnetic flux density distribution, for average radius. (a) Rotor yoke. (b) Magnet surface.

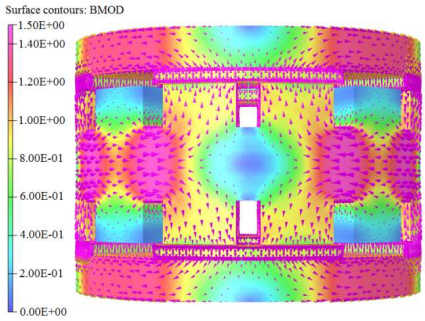

Figure 15. Flux path in stator yoke and teeth of designed slotted-TORUS AFPM motor.

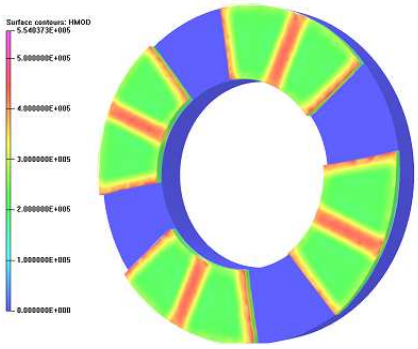

Figure 16. Magnetic potential for rotor and permanent magnets of designed slotted-TORUS AFPM motor.

of slots opening holes equals 15; however a few of these slot openings are hidden as there is no overlap between stator slots and permanent-magnet poles. In Fig. 13 stator yoke magnetic flux density is given along with stator teeth magnetic flux density at average radius. The maximum magnetic flux is 1.5 T which is the maximum allowable value (see Table 2), and 1.2 T average. Fig. 14 represents the magnetic flux density distribution at average radius for both rotor disc and permanent-magnets surface.

This flux density presentation enables comparison of results from FEA simulation with those obtained from sizing equation analysis. Table 8 lists maximum and average values of the magnetic flux density from the FEA simulation results as well as sizing equation investigation at various sections of the motor under no-load condition. The comparative results verify that the GA based sizing equation are in agree with FEA based computed results. The slotted-TORUS configuration utilized for this paper is a north-north magnet organization. The phase winding goes around the stator core, producing a short end-winding, thus reducing copper loss; however, the main flux must flow circumferentially along the stator core. Figs. 15 and 16 show the magnetic flux path in the stator yoke and the magnetic potential for the rotor permanent magnets, respectively.

7.1. Back-EMF Waveform

One of the objectives of this work is to design the AFPM motor with sinusoidal back-EMF waveform; in other words, the back-EMFs should be as sinusoidal as possible. Fig. 17 shows the 3-phase back-

EMFs at rated speed (1500 rpm) for 15-stator-slot AFPM synchronous machine for both with, and without permanent-magnet skewing; also FEA-calculated maximum and RMS value of back-EMF are displayed. The adoption of the fractional winding ($q = 5/4$) implies a beneficial filtering effect on the back-EMF waveform and avoid high distortion. This fact is confirmed in Fig. 18 (Fourier transform analysis of the back-EMF waveforms) by the amplitudes of 5th and 7th harmonics which are rather low, the most important harmonics well-known as the teeth harmonics of a $q = 1$ winding. It is also found that the THD drastically decreases from 8.1% to 2.5% with 9-degree optimized permanent-magnet skewing for 15-stator-slot AFPM synchronous machine.

7.2. Cogging Torque

When examining the torque performance, torque density and ripple must both be taken into account. Same as RFPM machines, AFPM machines also produce undesirable performance-affecting torque ripples. The main torque ripple sources include cogging torque, non-ideal back EMF waveforms, and saturated machine magnetic circuit [43].

During the motor design process, unwanted harmonics leading to non-ideal back-EMFs were minimized by creating strongly sinusoidal back-EMF waveform. The FEA base electromagnetic field simulation monitors the designed machine's magnetic circuit saturation in different sections of the motor. So, cogging torque can be a problem in machine design. It results from the permanent-magnet tendency to align itself at a minimum magnetic reluctance path between the rotor and stator. Permeance fluctuation in the slot opening resulting in rotor

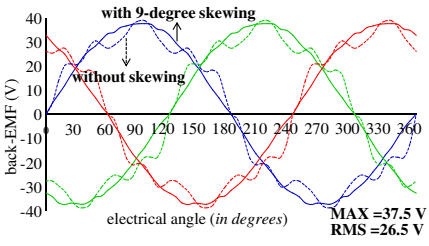

Figure 17. Three-phase back-EMFs at 1500 rpm, with and without, PM skewing for 15-stator-slot AFPM synchronous machine.

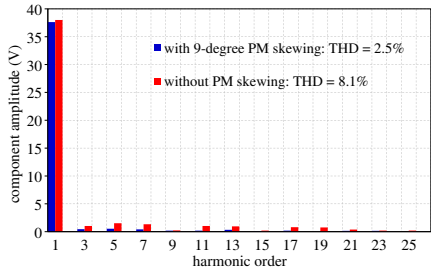

Figure 18. Comparison of back-EMF harmonic components, with and without PM skewing for the proposed 15-stator-slot machine.

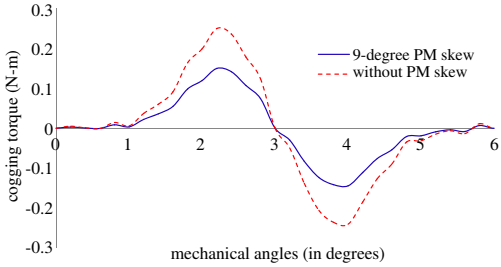

Figure 19. Cogging torque, with and without, PM skewing for the 15-slot machine.

tangential forces due to flux entering the teeth leads to an oscillatory output known as cogging torque. It introduces noise and vibration, both of which negatively influence the response of high-performance motion control, especially at low speed and light loads.

An effective, very simple and common method of reducing cogging torque is skewing. Skewing is either done by stator slots or rotor permanent magnets. Since the stator-slots skewing is relatively difficult to achieve in AFPM machines, the permanent magnets are skewed instead. Fig. 19 shows the 15-stator-slot AFPM machine's cogging torque, with and without permanent-magnet skewing. The pre-skewing peak cogging torque is around 0.25 nm and 9-degree skewed permanent magnet peak cogging torque is decreased to 0.15 nm (a 40% reduction). It is also found that the without skewing cogging torque is rather low as compared to full-pitch winding configuration due to fractional slot winding.

It is to be mentioned that mesh sensitivity analysis related to the computation of cogging torque is applied to be sure that increasing the number of elements does not affect the results.

It should be noted that the objective of this research is to design an electric motor with the highest possible power density, the most sinusoidal back-EMF waveform, the best heat removal, and reduced cogging torque. So, with the above mentioned significant reduced torque ripple, the objective of this research is satisfied; however, the 9-degree skew may still not be the optimal skew angle for cogging torque reduction and it may be further reduced using a different permanent-magnet skew angle or other techniques but the THD of the back-EMF will not be maintained minimum.

8. THERMAL FIELD ANALYSIS

The final designed motor also is subjected to heat transfer and fluid flow analysis. In order to run the simulation only half of the

entire motor is modeled in ANSYS-FLUENT due to the symmetrical configuration of the proposed design [40]. The simulation performed in this paper is based on the structured grids. This allows an increase in the solution accuracy and a lowering of the number of elements. In structured meshes, the node indexing follows the geometric position of the nodes, which leads to faster convergence [37] and higher accuracy than unstructured grids. The use of structured grid elements is also preferable in the viscous region of the domain [44]. This is valid for the whole domain in the case of internal flows.

Zero inlet total pressure and zero outlet static pressure boundary conditions are applied. A rotational speed of 1500 rpm is specified. The room temperature of 25°C is specified at the CFD model inlet. In order to get an accurate prediction of the temperature in various sections of the motor, solid components of the system are included in the model. The heat dissipation of the proposed motor cooling system is possible through both conduction and convection; however, the significant heat transfer is performed through convection. The conduction relates to solid parts and stationary fluid while convection relates to fluid movement. The fluid momentum and coarseness of solid's surface are the most effective factors in heat transfer between solid and fluid as it happens in solid-fluid interface. The boundary conditions in solid-fluid interface are calculated by couple method and hence the temperature values and coefficients of heat transfer are obtained through iteration method. The outer surface of the motor is exposed to stationary air. Therefore, the calculated coefficients of heat transfer are average values of solid and environment heat transfer coefficients. The other thermal boundary conditions are shown in Fig. 20, for a section of the three dimensional model. The appropriate boundary conditions are selected so that to simulate the actual heat transfer circumstances of the motor. It should be noted that in the motor design, in contrast with normal electrical machines, outer bearing is used. The mechanical advantages of this structure include improved balancing and cooling capability. It enables air to flow in through the center of rotor hollow and out through the air-gap.

A structural multi block meshing is used for all of domains such as stationary and rotational. Fig. 21 illustrates three dimensional meshing of model in Gambit by using cubical elements for calculating the circulations in the passages of the motor [45]. GAMBIT is used only to auto generate the finite volume mesh and simulation is analyzed with ANSYS-FLUENT software. The whole domain has been split into smaller elementary volumes connected to each other by sharing a common face. The grid is made of 3 million hexahedral elements. The clearance between stator and rotor contains about 2.2 million elements

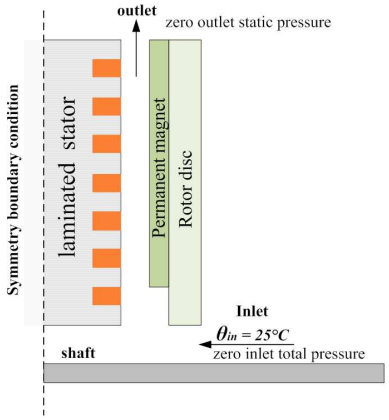

Figure 20. Thermal boundary conditions for a section of the model.

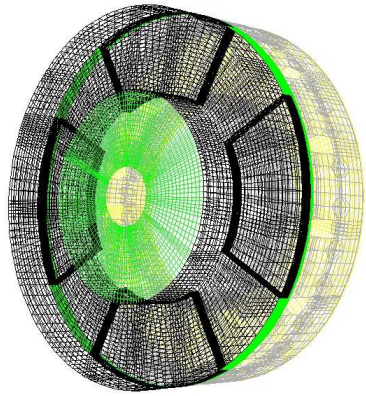

Figure 21. 3D auto-mesh generation by GAMBIT software (GAMBIT).

in total. The clearance has been meshed with 22 elements across the axial direction. Once the optimum number of mesh elements was determined to be 120956, it was seen that increasing the number of elements did not affect the results. This was confirmed by doubling the number of elements and observing no change in the simulation results. Finite volume analysis relies on type of elements, which affect the result significantly. In the simulations, TGrid-Map element, as an appropriate map structural element in simulation was chosen.

In ANSYS-FLUENT, the flow equations and the energy equation are solved separately: once the flow and turbulence equations converged, the energy equation is solved on the basis of obtained flow field. This method resulted in faster convergence. Simulations were run in ANSYS-FLUENT by using the (RANS) equations. The realizable κ-ε turbulent model was used for the closure of the system equations. The Enhanced Wall Treatment (EWT) which uses a two-layer approach was applied in FLUENT to model the near wall regions. This approach requires the non-dimensional wall distance $y+$ to be ~ 1 in the whole domain, although values of $y+ < 5$ are considered to be acceptable.

8.1. Heat Transfer

Figure 22 shows the temperature contour for both rotor and stator of the motor under full load condition, representing their thermal distribution. Heat dissipation of rotor and stator is possible through both conduction and convection. The heat generated in winding

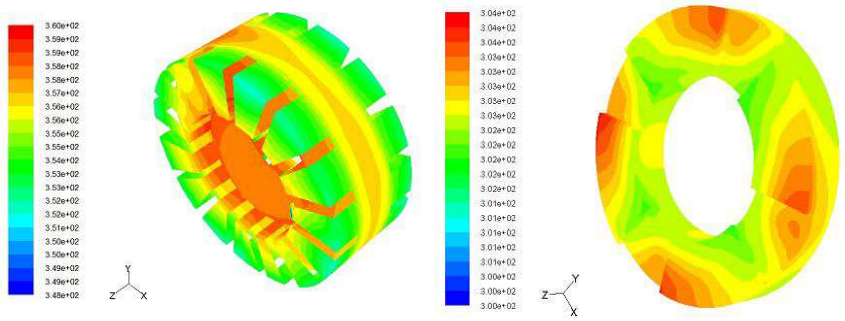

Figure 22. Temperature (°K) contour for both rotor and stator of the motor representing the thermal distribution. (a) Stator. (b) Rotor.

transfers linearly to the stator through conduction and is then conducted to the motor's body where the body surface cools by the environment. The convection is due to the air movement inside the air-gap because of skew permanent magnets mounted on the rotor surface acting like a fan. The amount of heat transfer on stator surface is almost fixed and is less than rotor's surface heat transfer amount. Fig. 22(a) shows the difference between the lowest and the highest temperatures are limited to 12°K and 360°K respectively. The significant temperature discrimination over the entire stator is due to lamination. However, the rotor small size and high metal conductivity cause the rotor temperature to have a low discrimination over the entire area as shown in Fig. 22(b): the difference between the lowest and the highest temperatures is limited to 4°K. There is no heat source on the rotor and the heat transfer is via convection through heated air in the motor air-gap. In steady-state rotation the rotor heating is uniform, except where there are juts on the rotor surfaces and exposed to more heated air flow. Therefore, temperature discrimination as the result of this phenomenon is very small. It is obvious that a temperature increase occurs proceeding from the inner radius towards the running clearance outlet. This is due to the air heating in the clearance. Maximum temperature occurred in stator areas adjunct with the winding coils especially in the areas nearer to inner radius due to higher winding per volume. In the other words, the maximum heat transfer coefficient is that in the rotor, where the radius is smallest.

8.2. Air Flow

Figure 23 shows the velocity (m/s) of the air inside the air-gap, motor's inlet and outlet for both velocity magnitude and radial velocity. The

velocity vectors on the $x = 0$ plane in Fig. 23(a) show the prevailing axial flow at the inlet. On this plane, as opposed to the case of the $x = 0$ plane, after the bend in the radial direction the cooling air passes through the groove between the magnets and the velocity magnitude is greater. The radial velocity in the back clearance is higher than in the front one because of its smaller size (Fig. 23(b)). A negative radial velocity region is visible at the front rotor inlet where the air intake occurs. Fig. 24 shows the colored path lines on rotor and permanent magnets showing a circulation. It's the result of low velocities in the

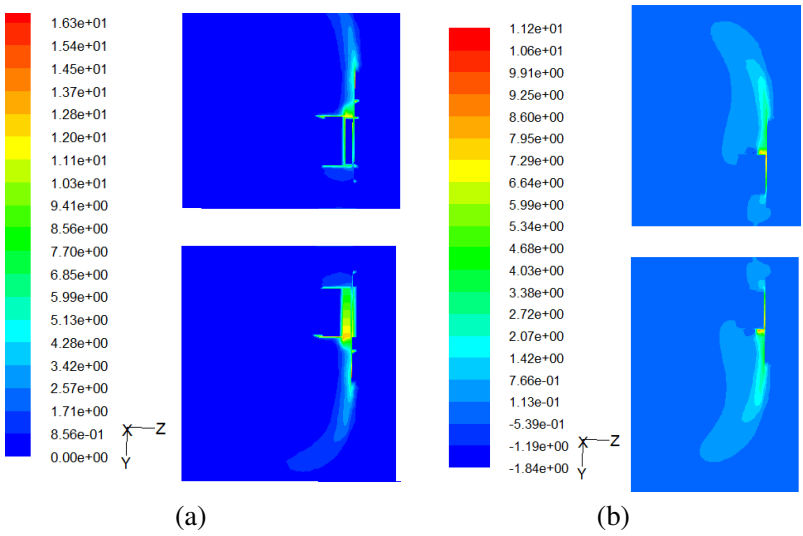

Figure 23. Contours of air velocity vectors (m/s) inside the air-gap. (a) Velocity magnitude. (b) Radial velocity.

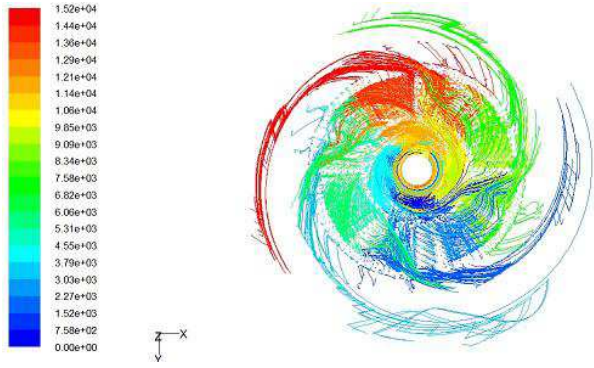

Figure 24. Path line on the rotor and permanent magnets surface.

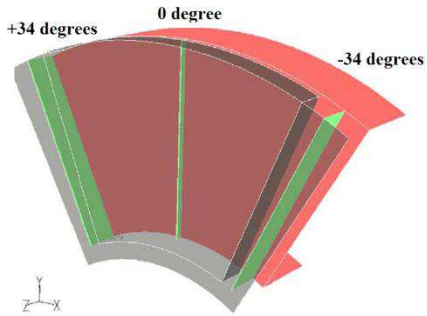

Figure 25. Velocity contours planes.

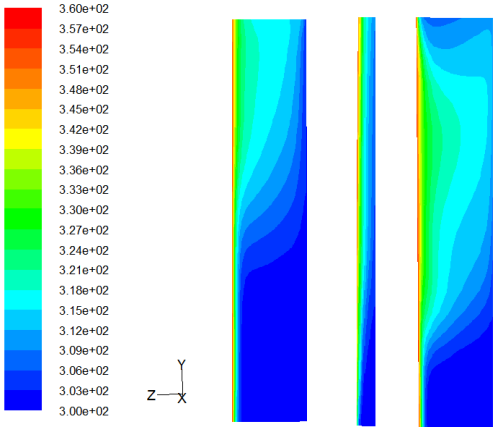

Figure 26. Velocity magnitude (m/s) on zy plane.

relevant inlet recess around the inner radius and vice versa higher velocities in the relevant outlet recess around the outer radius. The velocity magnitude contours have been obtained on the radial surfaces shown in Fig. 25 (at angles 34°, 0° and +34°). The region of the running clearance close to the rotor shows higher velocities than the one close to the stator (see Fig. 26). It is therefore desirable to have a low running clearance as it increases the turbulent mixing.

However, an excessively low running clearance could reduce the flow rate due to the excessive flow resistance. For given values of the permanent magnet depth and the rotational speed an increase of the clearance to a certain value results in the rise of the mass flow rate; however, further widening the clearance would not result in more increase of mass flow rate. This would reduce the radial velocity and the beneficial effect on the heat transfer coefficient. It is found that the highest temperature in the motor is 87°C under steady-state and

nominal conditions. This result is reasonable for a typical electric motor with similar size [46].

9. PERFORMANCE ANALYSIS

9.1. Load Test

Figure 27 shows the comparison of the torque-current characteristic for the proposed 15-stator-slot motor with and without permanent-magnet skewing. It shows almost the linear characteristics of the torque versus the load. It is also found that skewing design decreases the output torque. It is obvious that in various current the amount of torque for skew design is lower than that of without skewing.

Figure 28 shows the comparison of the torque-speed characteristic for the motor designs with and without permanent-magnet skewing. It shows that skewing design decreases the output torque, which is the usual case. It is also found that the maximum attainable speed for

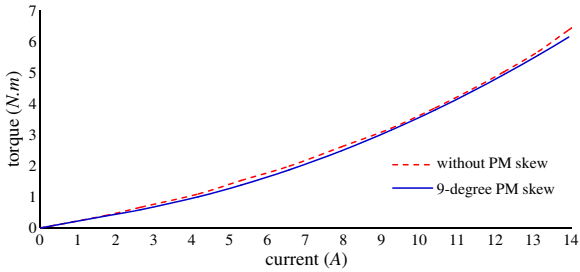

Figure 27. Current-torque characteristic, with and without, PM skewing for the proposed 15-stator-slot AFPM motor.

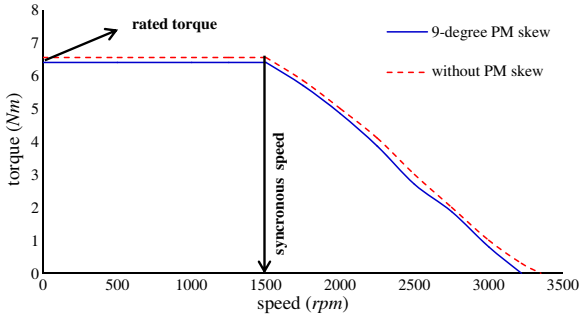

Figure 28. Speed-torque characteristic, with and without, PM skewing.

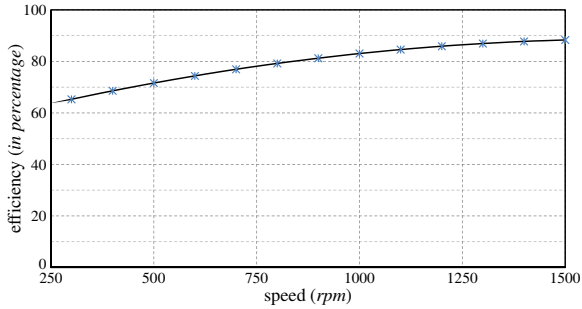

Figure 29. Efficiency versus speed at low-load condition (50% of full load) for the proposed 15-stator-slot, 9° PM skew AFPM synchronous machine.

the proposed 15-stator-slot AFPM synchronous motor are 3220 and 3350 rpm for skew PM and non-skew PM configuration, respectively.

9.2. Efficiency

It is vital to calculate the losses to extract the machine efficiency. The machine efficiency is given by:

$$\eta = \frac{P_{out}}{P_{out} + P_{cu} + P_{cor} + P_{rot}} \tag{31}$$

where P_{cor} and P_{cu} are calculated from equation below:

$$P_{cor} = P_h + P_e, \quad \text{and} \quad P_{cu} = R_s I^2 \tag{32}$$

Figure 29 shows the motor's efficiency at various speeds under low-load condition (50% of full load). Rotational loss (including windage and friction losses) is estimated [47]:

$$P_{rot} = \frac{1}{2} c_f \rho_r (\pi n^3) \left(D_o^5 - D_i^5\right) \tag{33}$$

where c_f is the friction coefficient, ρ_r the density of rotating part, and n the rotation speed (in rps). It is seen from the Fig. 29 that the motor maintains high efficiency even at low-load condition. The final optimal designed motor efficiency at full-load and rated condition is found as 90.5%.

10. CONCLUSION

An optimized design and performance analysis of an AFPM synchronous machine based on GA, FEA, and FVA has been presented

in this paper. The machine sizing equation, practical limitations, various structures, and winding configurations have been considered in the design process. The highest possible power density, minimum THD of the induced-EMF, best heat removal, and low cogging torque has been considered as the main design objectives. The GA has been used to minimize the size of a 1 kW, 3-phase, 50 Hz, 4-pole machine. A 3D-FEA software has been used to optimize and extract the characteristics of the machine based on the GA and FEA optimization. 10 superior design candidates have been found. Then the thermal investigation has been done for each design competent based on the 3d-FVA software and the best heat removal candidate has been selected as the final design for the machine. It is found from the FEA computed results that the designed motor meets the design specifications in terms of highest possible power density, minimum THD of induced-EMF, best heat removal and low cogging torque. It has also been found that the motor also maintains high efficiency at various speed conditions. Therefore, the proposed design method could be utilized to design the industrial AFPM synchronous machine of different ratings.

The fabrication process of the prototype AFPM synchronous machine is finished and experimental results will be presented in the next occasion.

APPENDIX A.

There are infinite possibilities for pole and slot count combinations similar to windings layouts. A particular method is used to place the coils [30]. The following assumptions are considered for winding design:

a) Three-phase motor.
b) All slots filled; the number of slots is a multiple of the number of phases (i.e., $N_s = k \times N_{ph}$).
c) Two coil-sides in each slot, the winding can be classified as double-layer winding.
d) Balanced-windings only, i.e., only pole and slot count combinations that result in back EMF of phases B and C being 120^{oE} offset from the back EMF of phase A.
e) Coils have equal numbers of turns, all spanning have equal number of slots, implying same-sized coils and therefore the same resistance and inductance.

Figure A1 shows the coil arrangements for 9, 12, 15, 18, 21, and 24 slots that gave the best sinusoidal waveforms. A, B, and C represent the phases, and + and − represent winding directions. The number of winding configuration options can also be increased by short-pitching

Slot No.	1	2	3	4	5	6	7	8	9
up	+A	-B	-A	+B	-C	-B	+C	-A	-C
down	+A	+C	-A	+B	+A	-B	+C	+B	-C

(a)

Slot No.	1	2	3	4	5	6	7	8	9	10	11	12
up	+A	-B	+C	-A	+B	-C	+A	-B	+C	-A	+B	-C
down	+A	-B	+C	-A	+B	-C	+A	-B	+C	-A	+B	-C

(b)

Slot No.	1	2	3	4	5	6	7	8	9	10	11	12	13	14	15
up	+A	-B	+C	-A	+B	+B	-C	+A	+A	-B	+C	-A	+B	-C	-C
down	-B	-B	+C	+C	-A	-C	-C	+A	-B	+C	-A	-A	+B	+B	+A

(c)

Slot No.	1	2	3	4	5	6	7	8	9	10	11	12	13	14	15	16	17	18
up	+A	-B	-B	+C	-A	+B	+B	-C	+A	+A	-B	+C	+C	-A	-A	+B	-C	-C
down	+A	-B	+C	+C	-A	-A	+B	-C	-C	+A	-B	-b	+C	-A	+B	+B	-C	+A

(d)

Slot No.	1	2	3	4	5	6	7	8	9	10	11	12	13	14	15	16	17	18	19	20	21
up	+A	-B	-B	+C	+C	-A	-A	+B	-C	-C	+A	+A	-B	-B	+C	-A	-A	+B	+B	-C	-C
down	+A	-B	-B	+C	+C	-A	+B	+B	-C	-C	+A	+A	-B	+C	+C	-A	-A	+B	+B	-C	+A

(e)

Slot No.	1	2	3	4	5	6	7	8	9	10	11	12	13	14	15	16	17	18	19	20	21	22	23	24
up	+A	+A	-B	-B	+C	+C	-A	-A	+B	+B	-C	-C	+A	+A	-B	-B	+C	+C	-A	-A	+B	+B	-C	-C
down	+A	+A	-B	-B	+C	+C	-A	-A	+B	+B	-C	-C	+A	+A	-B	-B	+C	+C	-A	-A	+B	+B	-C	-C

(f)

Figure A1. Stator winding configurations for 9, 12, 15, 18, 21, and 24 slots. (a) 9-slot double-layer stator winding (coil span = 2). (b) 12-slot double-layer stator winding (full-pitch). (c) 15-slot double-layer stator winding (coil span = 2). (d) 18-slot double-layer stator winding (coil span = 4). (e) 21-slot double-layer stator winding (coil span = 5). (f) 24-slot double-layer stator winding (full-pitch).

the fractional-slot structures. The 15-slot stator is designed with a 3-slot coil span, but a 2-slot coil span is also possible with easy reconfiguration. For an 18-slot structure, 3-slot coil span, and for 21-slot structure, both 3-slot and 4-slot coil spans can be considered. Considering the 13 stator winding configurations in Table A1, possible permanent magnet spans, their losses, back-EMF harmonic content and pulsating torque components are investigated. Efficiencies were relatively similar except at lower speeds, where the differences are more pronounced due to copper losses. The worst structure in terms of copper losses was found to be the 24-slot full-pitched; the best was the 15-slot, either 2 or 3.75, short-pitched structure.

Table A1. Possible winding configurations and number of stator slots in each pole, per phase.

configuration number	number of stator slots (N_s)	$\frac{\text{coil pitch}}{\text{pole pitch}}$	number of stator slots in each pole per phase (N_{spp})
1	9	2/2.25	0.75
2	12	2/3	1
3	12	full-pitch	1
4	15	2/3.75	1.25
5	15	3/3.75	1.25
6	18	3/4.5	1.5
7	18	4/4.5	1.5
8	21	3/5.25	1.75
9	21	4/5.25	1.75
10	21	5/5.25	1.75
11	24	4/6	2
12	24	5/6	2
13	24	full-pitch	2

ACKNOWLEDGMENT

The authors thank the University of Malaya for the High Impact Research Grant No. D000022- 6001 that funds the Hybrid Solar Energy Research Suitable for Rural Electrification.

REFERENCES

1. Matyas, A. R., K. A. Biro, and D. Fodorean, "Multi-phase synchronous motor solution for steering applications," *Progress In Electromagnetics Research*, Vol. 131, 63–80, 2012.
2. Zhao, W., M. Cheng, R. Cao, and J. Ji, "Experimental comparison of remedial single-channel operations for redundant flux-switching permanent-magnet motor drive," *Progress In Electromagnetics Research*, Vol. 123, 189–204, 2012.
3. Nguyen, Q. D. and S. Ueno, "Analysis and control of nonsalient permanent magnet axial gap self-bearing motor," *IEEE Tran. on Ind. Electron.*, Vol. 58, No. 7, 2644–2652, Jul. 2011.

4. Aydin, M., S. Huang, and T. A. Lipo, "Design, analysis, and control of a hybrid field-controlled axial-flux permanent-magnet motor," *IEEE Trans. on Ind. Electron.*, Vol. 57, No. 1, 78–87, Jan. 2010.
5. Kano, Y., T. Kosaka, and N. Matsui, "A simple nonlinear magnetic analysis for axial-flux permanent-magnet machines," *IEEE Tran. on Ind. Electron.*, Vol. 57, No. 6, 2124–2133, Jun. 2010.
6. Fei, W., P. C. K. Luk, and K. Jinupun, "Design and analysis of high-speed coreless axial flux permanent magnet generator with circular magnets and coils," *IET Electr. Power Appl.*, Vol. 4, No. 9, 739–747, Nov. 2010.
7. De Donato, G., F. Giulii Capponi, A. Rivellini, and F. Caricchi, "Integral-slot versus fractional-slot concentrated-winding axial-flux permanent-magnet machines: Comparative design, FEA, and experimental tests," *IEEE Trans. on Ind. Appl.*, Vol. 48, No. 5, 1487–1495, Sep./Oct. 2012.
8. Mahmoudi, A., N. A. Rahim, and W. P. Hew, "Axial-flux permanent-magnet motor design for electric vehicle direct drive using sizing equation and finite element analysis," *Progress In Electromagnetics Research*, Vol. 122, 467–496, 2012.
9. Caricchi, F., F. Maradei, G. De Donato, and F. G. Capponi, "Axial-flux permanent-magnet generator for induction heating Gensets," *IEEE Trans. on Ind. Electron.*, Vol. 57, No. 1, 128–137, Jan. 2010.
10. Gieras, J. F., et al., *Axial Flux Permanent Magnet Brushless Machines*, 2nd Edition, Springer-Verlag, New York, 2008.
11. Kurronen, P. and J. Pyrhonen, "Analytic calculation of axial-flux permanent-magnet motor torque" *IET Electr. Power Appl.*, Vol. 1, No. 1, 59–63, Jan. 2007.
12. Di Stefano, R. and F. Marignetti, "Electromagnetic analysis of axial-flux permanent magnet synchronous machines with fractional windings with experimental validation," *IEEE Tran. on Ind. Electron.*, Vol. 59, No. 6, 2573–2582, Jun. 2012.
13. Nguyen, T. D., K. J. Tseng, S. Zhang, and H. T. Nguyen, "A novel axial flux permanent-magnet machine for flywheel energy storage system: Design and analysis," *IEEE Tran. on Ind. Electron.*, Vol. 58, No. 9, 3784–3794, Sep. 2011.
14. Mahmoudi, A., S. Kahourzade, N. A. Rahim, and W. P. Ping, "Improvement to performance of solid-rotor-ringed line-start axial-flux permanent-magnet motor," *Progress In Electromagnetics Research*, Vol. 124, 383–404, 2012.

15. Di Gerlando, A., G. Foglia, and R. Perini, "Permanent magnet machines for modulated damping of seismic vibrations: Electrical and thermal modeling," *IEEE Trans. on Ind. Electron.*, Vol. 55, No. 10, 3602–3610, Oct. 2008.
16. Mahmoudi, A., S. Kahourzade, N. A. Rahim, W. P. Hew, and N. F. Ershad, "Slot-less torus solid-rotor-ringed line-start axial-flux permanent-magnet motor," *Progress In Electromagnetics Research*, Vol. 131, 331–355, 2012.
17. Huang, S., J. Luo, F. Leonardi, and T. A. Lipo, "A general approach to sizing and power density equations for comparison of electrical machines," *IEEE Trans. on Ind. Appl.*, Vol. 34, No. 1, 92–97, Jan./Feb. 1998.
18. Huang, S., J. Luo, F. Leonardi, and T. A. Lipo, "A comparison of power density for axial flux machines based on the general purpose sizing equation," *IEEE Trans. on Energy Convers.*, Vol. 14, No. 2, 185–192, Jan. 1999.
19. Aydin, M., S. Huang, and T. A. Lipo, "Design and 3D electromagnetic field analysis of non-slotted and slotted TORUS type axial flux surface mounted permanent magnet disc machines," *IEEE International Electric Machines and Drives Conf.*, 645–651, Jan. 2001.
20. Aydin, M., S. Huang, and T. A. Lipo, "Optimum design and 3D finite element analysis of non-slotted and slotted internal rotor type axial flux PM disc machines," *IEEE Power Engineering Society Summer Meeting*, 645–651, Jul. 2001.
21. Upadhyay, P. R. and K. R. Rajagopa, "FE analysis and computer-aided design of a Sandwiched axial-flux permanent magnet brushless DC motor," *IEEE Trans. on Magn.*, Vol. 42, No. 10, Oct. 2006.
22. Chan, T. F. and L. L. Lai, "An axial-flux permanent-magnet synchronous generator for a direct-coupled wind-turbine system," *IEEE Trans. on Energy Convers.*, Vol. 22, No. 1, Mar. 2007.
23. Di Gerlando, A., G. Foglia, M. F. Iacchetti, and R. Perini, "Axial flux PM machines with concentrated armature windings: Design analysis and test validation of wind energy generators," *IEEE Tran. on Ind. Electron.*, Vol. 58, No. 9, Sep. 2011.
24. Rostami, N., M. Feyzi, J. Pyrhonen, A. Parviainen, and V. Behjat, "Genetic algorithm approach for improved design of a variable speed axial-flux permanent-magnet synchronous generator," *IEEE Trans. Magn.*, 2012.
25. Chang, L., C. Liao, L.-L. Chen, W. Lin, X. Zheng, and Y.-L. Wu, "Design of an ultra-wideband power divider via the coarse-grained

parallel micro-genetic algorithm," *Progress In Electromagnetics Research*, Vol. 124, 425–440, 2012.

26. Gargama, H., S. K. Chaturvedi, and A. K. Thakur, "Design and optimization of multilayered electromagnetic shield using a real-coded genetic algorithm," *Progress In Electromagnetics Research B*, Vol. 39, 241–266, 2012.
27. Friedrich, G. and M. Kant, "Choice of drives for electric vehicles: A comparison between two permanent magnet AC machines," *IEE Proceedings Electric Power Applications*, Vol. 145, No. 3, 247–252, May 1998.
28. Jian, L., G. Xu, J. Song, H. Xue, D. Zhao, and J. Liang, "Optimum design for improving modulating-effect of coaxial magnetic gear using response surface methodology and genetic algorithm," *Progress In Electromagnetics Research*, Vol. 116, 297–312, 2011.
29. Zhu, X., W. Shao, J.-L. Li, and Y.-L. Dong, "Design and optimization of low RCS patch antennas based on a genetic algorithm," *Progress In Electromagnetics Research*, Vol. 122, 327–339, 2012.
30. Hanselman, D. C., *Brushless Permanent Magnet Motor Design*, McGraw-Hill, New York, 1994.
31. Bianchi, N., *Electrical Machine Analysis Using Finite Element*, Taylor & Francis, CRC Press, Florida, 2005.
32. Touati, S., R. Ibtiouen, O. Touhami, and A. Djerdir, "Experimental investigation and optimization of permanent magnet motor based on coupling boundary element method with permeances network," *Progress In Electromagnetics Research*, Vol. 111, 71–90, 2011.
33. Jian, L., G. Xu, Y. Gong, J. Song, J. Liang, and M. Chang, "Electromagnetic design and analysis of a novel magnetic-gear-integrated wind power generator using time-stepping finite element method," *Progress In Electromagnetics Research*, Vol. 113, 351–367, 2011.
34. Torkaman, H. and E. Afjei, "Comparison of three novel types of two-phase switched reluctance motors using finite element method," *Progress In Electromagnetics Research*, Vol. 125, 151–164, 2012.
35. Musolino, A., R. Rizzo, and E. Tripodi, "Tubular linear induction machine as a fast actuator: Analysis and design criteria," *Progress In Electromagnetics Research*, Vol. 132, 603–619, 2012.
36. Opera Version 14.0 User Guide, Vector Fields, 2011, http://www.c

obham.com.

37. Chung, T., *Computational Fluid Dynamics*, Cambridge University Press, 2010.
38. Giovani, A., "Numerical investigation of air flow and heat transfer in axial flux permanent magnet machines," Ph.D. Thesis, School of Engineering and Computer Science, Durham University, UK, Mar. 2010.
39. Versteeg, H. K. and W. Malalasekera, *An Introduction to Computational Fluid Dynamics: The Finite Volume Method*, Prentice Hall, Pearson, 2007.
40. ANSYS-FLUENT Finite Volume Simulation Software, ANSYS Inc, PA, Canonsburg, http://www.ansys.com.
41. Li, H., "Cooling of a permanent magnet electric motor with a centrifugal impeller," *International Journal of Heat and Mass Transfer*, Vol. 53, No. 4, 797–810, 2010.
42. Saari, J., "Thermal analysis of high-speed induction machines," Ph.D. Thesis, Helsinki University Technology, Helsinki, Finland, Jan. 1998.
43. Wu, L. J., Z. Q. Zhu, D. A. Staton, M. Popescu, and D. Hawkins, "Comparison of analytical models of cogging torque in surface-mounted PM machines," *IEEE Tran. on Ind. Electron.*, Vol. 59, No. 6, 2414–2425, Jun. 2012.
44. Blazek, J., *Computational Fluid Dynamics: Principles and Applications*, Elsevier Science Ltd, 2005.
45. GAMBIT Software Tools Version 0.2010.09.01, available: http://www.gambit-project.org.
46. Marignetti, F., V. Delli Colli, and Y. Coia, "Design of axial flux PM synchronous machines through 3-D coupled electromagnetic thermal and fluid-dynamical finite-element analysis," *IEEE Trans. on Ind. Electron.*, Vol. 55, No. 10, 3591–3601, Oct. 2008.
47. Wang, R. J., M. J. Kamper, and K. V. D. Westhuizen, "Optimal design of a coreless stator axial flux permanent magnet generator," *IEEE Trans. on Magn.*, Vol. 41, No. 1, 55–64, Jan. 2005.